

## GEOPHYSICS®

**Effect of brine-CO<sub>2</sub> fracture flow on velocity and electrical resistivity of naturally fractured tight sandstones**

Journal:	<i>Geophysics</i>
Manuscript ID	GEO-2017-0077.R3
Manuscript Type:	Deciphering fractured rock properties from seismic wavefields
Date Submitted by the Author:	10-Oct-2017
Complete List of Authors:	Nooraiepour, Mohammad; Universitetet i Oslo, Department of Geosciences Bohloli, Bahman; Norwegian Geotechnical Institute (NGI) Park, Joonsang; Norwegian Geotechnical Institute (NGI) Sauvin, Guillaume; Norwegian Geotechnical Institute (NGI) Skurtveit, Elin; Norwegian Geotechnical Institute (NGI) Mondol, Nazmul; Universitetet i Oslo, Department of Geosciences; Norwegian Geotechnical Institute (NGI)
Keywords:	compressional wave (P-wave), electrical/resistivity, fractures, permeability, monitoring
Area of Expertise:	Rock Physics, Interdisciplinary Studies

SCHOLARONE™  
Manuscripts

**Effect of brine-CO<sub>2</sub> fracture flow on velocity and electrical resistivity of naturally fractured tight sandstones**

Mohammad Nooraiepour <sup>1,\*</sup>, Bahman Bohloli <sup>2</sup>, Joonsang Park <sup>2</sup>, Guillaume Sauvin <sup>2</sup>,  
Elin Skurtveit <sup>2</sup>, Nazmul Haque Mondol <sup>1,2</sup>

1 Department of Geosciences, University of Oslo (UiO), P.O. Box 1047 Blindern, 0316 Oslo, Norway

2 Norwegian Geotechnical Institute (NGI), P.O. Box 3930 Ullevaal Stadion, 0806 Oslo, Norway

\* Corresponding author, mohammad.nooraiepour@geo.uio.no

Original paper date of submission: 1 February 2017

Revised paper date of submission: 10 October 2017

1  
2  
3  
4  
5  
6  
7  
8  
9  
10  
11  
12  
13  
14  
15  
16  
17  
18  
19  
20  
21  
22  
23  
24  
25  
26  
27  
28  
29  
30  
31  
32  
33  
34  
35  
36  
37  
38  
39  
40  
41  
42  
43  
44  
45  
46  
47  
48  
49  
50  
51  
52  
53  
54  
55  
56  
57  
58  
59  
60

## ABSTRACT

Fracture networks inside geological CO<sub>2</sub> storage reservoirs can serve as primary fluid flow conduit, particularly in low-permeability formations. While some experiments focused on the geophysical properties of brine- and CO<sub>2</sub>-saturated rocks during matrix flow, geophysical monitoring of fracture flow when CO<sub>2</sub> displaces brine inside the fracture seems to be overlooked. We have conducted laboratory geophysical monitoring of fluid flow in a naturally fractured tight sandstone during brine and liquid CO<sub>2</sub> injection. For the experiment, the low-porosity, low-permeability naturally fractured core sample from the Triassic De Geerdalen Formation was acquired from the Longyearbyen CO<sub>2</sub> storage pilot at Svalbard, Norway. Stress-dependence, hysteresis and the influence of fluid-rock interactions on fracture permeability were investigated. The results suggest that in addition to stress level and pore pressure, mobility and fluid type can affect fracture permeability during loading and unloading cycles. Moreover, the fluid-rock interaction may impact volumetric strain and consequently fracture permeability through swelling and dry out during water and CO<sub>2</sub> injection, respectively. Acoustic velocity and electrical resistivity were measured continuously in the axial direction and three radial levels. Geophysical monitoring of fracture flow revealed that the axial P-wave velocity and axial electrical resistivity are more sensitive to saturation change than the axial S-wave, radial P-wave, and radial resistivity measurements when CO<sub>2</sub> was displacing brine, and the matrix flow was negligible. The marginal decreases of acoustic velocity (maximum 1.6% for axial V<sub>p</sub>) compared to 11% increase in axial electrical resistivity suggest that in the case of dominant fracture flow within the fractured tight reservoirs, the use of electrical resistivity methods have a clear advantage compared to seismic methods to monitor CO<sub>2</sub> plume. The knowledge learned from

such experiments can be useful for monitoring geological CO<sub>2</sub> storage where the primary fluid flow conduit is fracture network.

INTRODUCTION

Carbon capture and storage (CCS) in geological formations is a crucial near-term solution to mitigate climate change caused by the atmospheric anthropogenic carbon dioxide (CO<sub>2</sub>). Ensuring safe and secure subsurface CO<sub>2</sub> storage and tracking how the injected CO<sub>2</sub> moves within the reservoir rocks are among the key questions regarding the CCS projects (Arts and Winthaege, 2005). In a full-scale geological CO<sub>2</sub> sequestration project millions of tons must be stored underground, securing of which requires coupled hydraulic–geomechanical–geochemical analyses (Rutqvist, 2012). Moreover, geophysical monitoring is a necessity for establishing a reliable long-term operation (Braathen et al., 2012).

Fracture networks inside geological CO<sub>2</sub> storage reservoirs can serve as the primary fluid flow conduit, particularly in low-permeability formations. The state of stress influences the fluid flow in fractures through changing the void space between the two fracture surfaces in partial contact. Initial stress field and changes in stress regimes during CO<sub>2</sub> injection, therefore, affect the hydraulic and mechanical properties of the rock mass (Pyrak-Nolte and Nolte, 2016). While it is the size and spatial distribution of fracture apertures that control the volumetric flow rate and hydraulic properties, it is the asperities that define the mechanical properties of fractures (Pyrak-Nolte and Nolte, 2016). The asperities are the discrete contact points between the fracture surfaces. In addition to hydraulic and mechanical properties, changes in fluid saturation impact the geophysical responses (acoustic and electric properties) of fractured CO<sub>2</sub> storage reservoirs (Arts and Winthaege, 2005).

1  
2  
3  
4  
5  
6  
7  
8  
9  
10  
11  
12  
13  
14  
15  
16  
17  
18  
19  
20  
21  
22  
23  
24  
25  
26  
27  
28  
29  
30  
31  
32  
33  
34  
35  
36  
37  
38  
39  
40  
41  
42  
43  
44  
45  
46  
47  
48  
49  
50  
51  
52  
53  
54  
55  
56  
57  
58  
59  
60

## Geophysics

4

The literature related to hydraulic and geological aspects of fractured rocks is broad and extensive since researchers with diverse backgrounds have performed a vast range of experimental, theoretical, numerical and field investigations (Berkowitz, 2002). Several researchers studied the average fracture displacement, fracture void area and fracture permeability as a function of applied stress (such as Pyrak-Nolte and Morris, 2000; Roger, 2003; Huo and Benson, 2015). They reported a nonlinear and inelastic behavior of fracture permeability under loading and unloading cycles. Since the fracture voids are more crack-like compared to the pores in a porous medium, the geometry of areas in contact changes more rapidly and shows higher stress sensitivity in response to the applied stresses (National Research Council, 1996). Although it is demonstrated that normal and shear stresses influence fracture permeability (National Research Council, 1996; Roger, 2003), variations in fracture permeability at low- and high-stress levels and at different pore pressures for liquid and gaseous phase can be investigated further. The results would provide insights for evaluation of injectivity for different CO<sub>2</sub> storage candidates at different depth levels. The influence of fluid type and rock-fluid interaction (both mechanical and chemical impacts) on fracture permeability for CO<sub>2</sub> and water should be considered too because it may alter flow pathways and consequently permeability (National Research Council, 1996; Kampman et al., 2014; Blaisonneau et al., 2016).

By considering fluid flow through matrix, a number of research conducted geophysical measurements to investigate properties of brine- and CO<sub>2</sub>-saturated sandstones (such as Lei and Xue, 2009; Nakatsuka et al., 2010; Alemu et al., 2013; Chen et al., 2013; Nakagawa et al., 2013; Omolo, 2015; Tran, 2015; Falcon-Suarez et al., 2016a). Laboratory measurements showed that resistivity of porous sandstones is profoundly influenced (increased to about five times) when CO<sub>2</sub> displaced brine in the matrix (Nakatsuka et al., 2010; Alemu et al., 2013; Omolo, 2015;

Geophysics

Tran, 2015). Moreover, while theoretical models could estimate CO<sub>2</sub> saturation for clean, homogeneous rocks, they failed to provide accurate results for heterogeneous shaly reservoir rocks (Nakatsuka et al., 2010; Alemu et al., 2013). It is demonstrated that variations in porosity, matrix heterogeneity and the layering relative to flow direction can considerably influence the CO<sub>2</sub> distribution pattern during drainage (Lei and Xue, 2009; Alemu et al., 2013; Nakagawa et al., 2013; Falcon-Suarez et al., 2016a). Acoustic velocity indicates a less sensitivity to fluid distribution pattern compared to resistivity (Alemu et al., 2013). During drainage of brine by CO<sub>2</sub>, P-wave velocity ( $V_p$ ) decreased about 5% to 15% (Lei and Xue, 2009; Chen et al., 2013; Falcon-Suarez et al., 2016a; Omolo, 2015; Tran, 2015). Lei and Xue (2009) documented that when CO<sub>2</sub> displaced brine matrix saturation, about 7.5%, 12% and 14.5% decrease in  $V_p$  is expected for gaseous, liquid and supercritical CO<sub>2</sub>, respectively.

Despite the extensive studies on the geophysical properties of brine- and CO<sub>2</sub>-saturated rocks, there is no published research on the geophysical monitoring of CO<sub>2</sub> fracture flow when the contribution of matrix flow is negligible. Lessons learned from the concurrent fluid flow and geophysical measurements on reservoir analog fractured samples can be particularly valuable for monitoring of CO<sub>2</sub> plume movements during CO<sub>2</sub> injection in fractured reservoirs. In addition, comparing sensitivity and detectability of acoustic and electrical resistivity techniques during dominant fracture flow provides valuable insights for geological CO<sub>2</sub> storage.

This paper provides an experimental study of a naturally fractured tight sandstone core retrieved from the De Geerdalen Formation (the target CO<sub>2</sub> storage reservoir for the CO<sub>2</sub> Pilot project, Longyearbyen, Svalbard, Norway). The core sample was selected such to have negligible matrix permeability (minimal to non-existent matrix flow). The main research

1  
2  
3  
4  
5  
6  
7  
8  
9  
10  
11  
12  
13  
14  
15  
16  
17  
18  
19  
20  
21  
22  
23  
24  
25  
26  
27  
28  
29  
30  
31  
32  
33  
34  
35  
36  
37  
38  
39  
40  
41  
42  
43  
44  
45  
46  
47  
48  
49  
50  
51  
52  
53  
54  
55  
56  
57  
58  
59  
60

Geophysics

6

objective is geophysical monitoring (acoustic velocity and electrical resistivity) of dominant fracture flow during brine and liquid CO<sub>2</sub> injection. In addition, stress-dependence, hysteresis, and effect of fluid-rock interaction on fracture permeability were studied. The outcomes may provide a better understanding of the dominant fracture flow, and changes in electrical resistivity and acoustic velocity during geological CO<sub>2</sub> storage.

## MATERIALS AND METHODS

### Reservoir and core sample properties

In the Longyearbyen CO<sub>2</sub> storage pilot project, it was planned to inject CO<sub>2</sub> into the Triassic–Jurassic tight but fractured sandstone reservoirs at a depth of 700–1000 m beneath the High Arctic community of Longyearbyen, Svalbard, Norway. The project aimed to contribute to a better understanding of CO<sub>2</sub> migration in the subsurface, and to reduce the local anthropogenic CO<sub>2</sub> emissions (Braathen et al., 2012). The reservoir sandstone units at Longyearbyen are characterized with moderate secondary porosity and very low matrix permeability (Ogata et al., 2014). The in situ water injection tests documented extensive lateral fluid flow within the reservoir sandstones through the pre-existing fracture networks (Ogata et al., 2014).

The naturally fractured core sample was obtained from a depth of 773.37 m in Borehole Dh2, a vertical well, 850 m deep in the Longyearbyen CO<sub>2</sub> storage pilot project at the Arctic Norway (Svalbard). According to the stratigraphic logs and correlation between two drilled holes Dh2 and Dh4 (Braathen et al., 2012), the selected core sample was found to be part of the Late Triassic De Geerdalen Formation. The De Geerdalen Formation represents marginal marine to lagoonal and delta plain deposits (Mørk et al., 1999). Detailed logging of selected well within the

Geophysics

Longyearbyen research laboratory identified a coarsening upwards sandstones capped by carbonates and shales (Braathen et al., 2012). The whole-rock (bulk) mineralogical analysis of sandstone units showed that the reservoir sandstone consists mainly of quartz, feldspar and rock fragments with minor amounts of clay, carbonate as well as opaque minerals like pyrite (Mørk, 2013). The tested sample in this study is a well-cemented sandstone (extensive quartz cement, in addition to some carbonate cement), which resulted in an extremely low matrix permeability (Table 1, < 0.001 mD) and negligible matrix flow (Ogata et al., 2014). Figure 1 presents optical micrographs of extensively quartz-cemented low-porosity and low-permeability De Geerdalen sandstone. Moreover, significant porosity heterogeneity was reported in the studied sequence (Braathen et al., 2012; Magnabosco et al., 2014). As it is observed in Figure 1 and demonstrated in Figure 4, the thin shaly intervals and cementation caused large variations in porosity and contributed to significant heterogeneity. The sample was dry before testing. Table 1 presents properties of the tested core plug.

The identified fractures in the core samples and outcrop observations are considered as the dominant flow conduits (Ogata et al., 2014). The selected sandstone intervals in the De Geerdalen Formation show an average porosity in the range of 4-13 % and mean permeability of 0.03-0.07 mD with some local zones up to 2 mD (Farokhpoor et al., 2014). The reported values for stiffness and tensile strength of the sandstone intervals are presented in Table 2 (Bohloli et al., 2014). The unconfined compressive strength (UCS) and tensile strength show substantial values considering the present burial depth. The observed high strength is associated with the deep burial (around 3.5 to 4.5 km) of De Geerdalen sandstones that caused chemical compaction and extensive cementation in these reservoir horizons sandstones before exhumed at present depth.

1  
2  
3  
4  
5  
6  
7  
8  
9  
10  
11  
12  
13  
14  
15  
16  
17  
18  
19  
20  
21  
22  
23  
24  
25  
26  
27  
28  
29  
30  
31  
32  
33  
34  
35  
36  
37  
38  
39  
40  
41  
42  
43  
44  
45  
46  
47  
48  
49  
50  
51  
52  
53  
54  
55  
56  
57  
58  
59  
60



### **X-ray micro-computed tomography**

A Nikon micro-computed tomography (CT) system (XT H 225 LC) equipped with a 225 kV microfocus X-ray tube was used for imaging the core plug before and after the tests. The spot size of the X-ray beam was about 3  $\mu\text{m}$ , enabling a 50  $\mu\text{m}$  voxel resolution. Each CT-scan consisted of 1000 2D X-ray projection images taken at different angles between 0° and 360° rotation of the sample. The projections in each scan were TIFF formatted 16-bit images of 2000  $\times$  2000 pixels. Stacks of the projection images were used to reconstruct 3D volume images with a voxel size of about 50  $\times$  50  $\times$  50  $\mu\text{m}$ . The 3D images were reconstructed using VGStudio MAX software (Volume Graphics Company). After reconstruction, the voxels in the 3D volume were assigned a gray value (CT number) that is proportional to the X-ray attenuation of the material. The X-ray attenuation is dependent on the density and chemical composition of the material in each voxel. Pre-processing of the reconstructed volumes consisted of correction for beam hardening and ring artifact attenuation. Subsequently, a near neighbor search algorithm combined with connectivity analysis was applied to estimate the fracture aperture (Fig. 4).

### **Experimental setup**

Two different core flooding systems were utilized in this study. The fluid flow system at the Norwegian Geotechnical Institute (NGI) is equipped with geophysical measurement system (ultrasonic velocity and electrical resistivity), while the core flooding system at the University of Oslo (UiO) is specialized for multiphase flow experiments.

Figure 2 depicts a schematic of the experimental setup at NGI. The experimental setup is designed around a fluid flow unit with an isotropic confining pressure. The confining fluid

Geophysics

(polysiloxane fluid, SF1147 Momentive) was delivered through a computer-controlled screw pump (GDS pressure-volume controller). The fluid injection system consisted of two computer-controlled screw pumps (GDS pressure-volume controller) and one dual-cylinder syringe pump (Teledyne Isco, 260D), which controlled fluid flow rate and pore pressure within the system (Fig. 2). The brine (35000 ppm NaCl salt concentration) injection was performed using the screw pump, while liquid CO<sub>2</sub> (grade 5.2, AGA Company) was injected by the syringe pump. The backpressure was controlled at the outlet using another computer-controlled GDS pressure-volume controller. Three pressure sensors monitored the fluid pressure at the inlet, outlet and the confining volume throughout the test. The rubber sleeve, isolating the sample from the confining fluid, was equipped with sensors for geophysical measurements. As it is demonstrated in Figure 3, three levels of P-wave piezo-ceramic crystals and resistivity sensors were embedded on the nitrile sleeve along the sample height that enabled us to monitor the radial P-wave velocity ( $V_{pr}$ ) and the radial resistivity ( $R_r$ ). In addition, two piezoelectric transducers at the top cap and base plate were used to measure axial P- and S-wave velocities ( $V_{pa}$  and  $V_{sa}$ ), and axial resistivity ( $R_a$ ) during the experiment. Moreover, two diametrically opposed LVDTs (linear variable displacement transducers) and one radial LVDT were directly mounted on the membrane sleeve, which measured axial and radial deformations. The LVDTs recorded the deformation with a precision of 0.25-0.5 micrometers. The position of radial deformation sensor is demonstrated in Figure 3a. Figure 3 also illustrates the micro-CT image of fracture surface inside the sleeve, and its relative position with respect to the three pairs of radial sensors.

The other experimental apparatus was HPHT core flooding system (manufactured by Core Laboratories) at UiO, which was used for measurement of stress-dependence and hysteresis of fracture permeability. It comprises Hassler-type stainless steel core holder, two syringe pumps

1  
2  
3  
4  
5  
6  
7  
8  
9  
10  
11  
12  
13  
14  
15  
16  
17  
18  
19  
20  
21  
22  
23  
24  
25  
26  
27  
28  
29  
30  
31  
32  
33  
34  
35  
36  
37  
38  
39  
40  
41  
42  
43  
44  
45  
46  
47  
48  
49  
50  
51  
52  
53  
54  
55  
56  
57  
58  
59  
60

(inlet and outlet), back pressure regulator, two-phase separator, and gas mass flow controllers (three different ranges). The system allows for automated management of hardware resources and data acquisition. For a detailed description of UiO HPHT core flooding system, the reader is referred to Moghadam et al. (2016).

### Permeability measurements

To measure absolute permeability, we performed steady-state flooding tests at constant pressure gradient condition and calculated permeability using Darcy's law. Since the reported matrix permeability of the De Geerdalen core plug is several orders of magnitude lower than the measured permeability in the present study (Braathen et al., 2012; Farokhpoor et al., 2014), the permeability values during the flooding experiments are attributed to the fracture permeability. At the pore pressure levels of the experiment, the slippage effect is highly suppressed and therefore not considered here (Firouzi and Wilcox, 2013, Huo and Benson, 2015). All the experiments were carried out at the room temperature of 19-21°C. Potential geochemical reactions between the rock and injected fluids considered unlikely at the experimental time scale and pressure-temperature conditions.

### Ultrasonic velocity and electrical resistivity measurements

The pulse transmission technique was used to measure P- and S-wave velocities throughout the test. The technique consists of measuring the travel time of an acoustic signal through a sample of known dimension. The ultrasonic propagation system is made up of a pulse generator, a receiver, and a digital oscilloscope for recording the signals. A resonant frequency of 500 kHz was used to generate and receive ultrasonic signals. First-arrival times were picked from the

1 recorded waveforms using the NGI's in-house software (Time Picker) and were converted to  
 2 ultrasonic velocity. The details of pulse transmission technique and velocity error analysis were  
 3 presented in Nooraiepour et al. (2017). While sampling interval for digitizing the ultrasonic  
 4 waveform was the precision limiting factor (0.05  $\mu$ s for axial and 0.02  $\mu$ s for radial signals), the  
 5 absolute error in acoustic measurements was estimated as 30 m/s for  $V_{pa}$ , 10 m/s for  $V_{sa}$  and 20  
 6 m/s for  $V_{pr}$  (about 0.63%, 0.28% and 0.43% relative error, respectively). To measure the  
 7 electrical resistivity along the sample, the top cap was electrically separated from the bottom  
 8 pedestal and the rest of the cell using PEEK tubing. The use of PEEK tubing for pore fluid flow  
 9 inside the cell avoided leakage of electrical current during the measurements. In addition to the  
 10 axial measurement, the resistivity was measured radially on three different levels. The electrical  
 11 signal was sent through the sample by applying an input voltage of 10 volts at 1 kHz frequency.  
 12 For each measurement, ten different recordings were acquired and averaged. During the  
 13 experiments, the electrical resistance (ohm) was measured in the laboratory, and then it was  
 14 converted to electrical resistivity (ohm-meter). To quantify the radial resistivity and to account  
 15 for variations due to anisotropy and tortuosity, a correction factor was used to obtain the true  
 16 radial resistivity. Following the procedure introduced by Wang et al. (2009) and Choi et al.  
 17 (2017), numerical simulation and iteration were performed to find the correction factor.

**Experimental procedures**

18 To study stress-dependence of fracture permeability, we performed flow experiments using  
 19 gaseous CO<sub>2</sub> and deionized water (Milli-Q water). The core sample was initially considered dry  
 20 and was saturated with CO<sub>2</sub> (after vacuuming) within the Hassler-type core holder to measure  
 21 permeability to CO<sub>2</sub>. Subsequently, after completing the CO<sub>2</sub> cycles, the core plug was  
 22  
 23  
 24  
 25  
 26  
 27  
 28  
 29  
 30

## Geophysics

12

1  
2  
3  
4  
5  
6  
7  
8  
9  
10  
11  
12  
13  
14  
15  
16  
17  
18  
19  
20  
21  
22  
23  
24  
25  
26  
27  
28  
29  
30  
31  
32  
33  
34  
35  
36  
37  
38  
39  
40  
41  
42  
43  
44  
45  
46  
47  
48  
49  
50  
51  
52  
53  
54  
55  
56  
57  
58  
59  
60

vacuumed and dried at 60°C, and then saturated with deionized water under vacuum for measuring liquid permeability. In these flow measurements, while pore pressure was kept constant in each cycle (2, 3 and 4 MPa), the confining pressure was increased stepwise (3 MPa increments) up to 24 MPa. The pore pressure was calculated as the average of fluid pressure at the inlet and the outlet. The pressure gradient across the sample was also set to be equal to the pore pressure. After finishing one loading cycle, we conducted permeability measurements during the unloading cycle. Finally, the confining pressure was completely released, and the sample was left overnight.

While performing fluid flow using gaseous CO<sub>2</sub> and deionized water, we noticed a time-dependent and fluid-dependent behavior. To differentiate between the time-dependent and fluid-dependent effects and to characterize the phenomenon better, we designed and conducted a sequence of constant injection rate experiments. First, the core sample was vacuumed and dried to bring it to its original state before the experiment. Subsequently, water (deionized), CO<sub>2</sub> (gas), and oil (Marcol 52) were continuously flooded (1 cm<sup>3</sup>/min) through the sample one after another, each for 48 hours. The pore pressure and pressure gradient were set to be at 2 MPa. While our study was focused on water and CO<sub>2</sub>, we used oil (Marcol 52) to study the behavior of fracture permeability when least interaction of rock-fluid or changes in volumetric strain due to the injectant was expected. The core sample was not dried nor cleaned when injection of each fluid was completed to evaluate and compare the effect of different fluids and potential rock-fluid interaction on fracture permeability.

To assess the effect of dominant fracture flow on geophysical properties of low-porosity, low-permeability sandstones, we performed another core flooding experiment on the De

Geerdalen core plug. The core sample was initially cleaned, vacuumed and dried to bring it to its original state. The acoustic velocity and electrical resistivity were continuously recorded through the experimental phases. The test consisted of four phases (Fig. 8a): (a) phase 1 was the consolidation and brine saturation phase, where the confining pressure and pore pressure were simultaneously increased to 12 MPa and 9 MPa, respectively while the differential pressure was kept constant at 3 MPa; (b) flooding of brine through the fracture was carried out in the second phase, while the confining pressure and pore pressure was kept constant at 12 MPa and 9 MPa, respectively; (c) in phase 3, differential pressure (confining pressure minus pore pressure) was raised from 3 MPa to 7.5 MPa by increasing confining pressure to 16.5 MPa; and (d) during phase 4 (after 27000 minute), drainage core flooding was conducted by injecting liquid CO<sub>2</sub> and displacing brine. In the phase 1-3, brine was injected from the bottom of the sample, while during the drainage phase (phase 4) liquid CO<sub>2</sub> was flooded from the top.

## RESULTS

### Characterization of fracture surface

An optical image, pre-test x-ray micro-CT scan of the core plug and the fracture surface are depicted in Figure 4. Moreover, pre- and post-test plots of the fracture aperture are demonstrated in Figures 4d and 4e. The sample contains a vertical mode I fracture with no signs of shear movement along the fracture plane. The micro-CT image (Fig. 4b) shows a heterogeneous quartz dominated sandstone in the upper part of the sample and a siltier to shaly matrix at the bottom. The initial fracture aperture shows an open fracture with a dominated aperture about 150 μm, and some local contact areas and a maximum aperture of around 350 μm (Fig. 4d). According to the classification of fractures from core and outcrop observations of the De Geerdalen Formation by

Ogata et al. (2014), the tested fracture is characterized within a steep (vertical) fracture system associated with sandstone intervals and related to the last phase of tectonic uplift. This type of fracture, described as a hairline fracture in the core, often contains oxidization that indicates recent flow through the fracture. The aforementioned fracture system is considered an important fracture type for reservoir flow in the Longyearbyen CO<sub>2</sub> storage pilot project.

### **Stress-dependence and hysteresis of fracture permeability**

The experimental results for fracture permeability to gaseous CO<sub>2</sub> and deionized water are plotted in linear scale in Figures 5a and 5b, respectively. The measured fracture permeability varies in a range between 0.1 mD to less than 0.01 mD (Fig. 5). While the first data points in each cycle indicate a different confining pressure due to constraints imposed by different injection pressures, the rest of the measurements reflect the same confining pressure levels (Fig. 5). Figure 5 demonstrates a power law decrease of fracture permeability with the increase of confining pressure at a given pore pressure. The permeability drop is pronounced in early loading stages. Moreover, an increase in permeability is observed with increasing pore pressure from 2 MPa to 3 MPa and then to 4 MPa. The relative increase of fracture permeability is higher when pore pressure increased from 3 MPa to 4 MPa than that from 2 MPa to 3 MPa (Fig. 5). In addition, the higher the pore pressure, the lower the fracture permeability reduction during the loading cycle. When the naturally fractured sample was compressed, the fracture permeability decreased to 6-12% of the original value at the beginning of loading cycle. Figure 5 illustrates a gentler permeability reduction and higher values for gaseous CO<sub>2</sub> compared to DI-water. Figure 5b shows that the decrease in permeability around 16 MPa confining pressure is more significant for DI-water and the reductions afterward are relatively small. Moreover, for confining pressures

1  
2  
3  
4  
5  
6  
7  
8  
9  
10  
11  
12  
13  
14  
15  
16  
17  
18  
19  
20  
21  
22  
23  
24  
25  
26  
27  
28  
29  
30  
31  
32  
33  
34  
35  
36  
37  
38  
39  
40  
41  
42  
43  
44  
45  
46  
47  
48  
49  
50  
51  
52  
53  
54  
55  
56  
57  
58  
59  
60

above 16 MPa, the permeability to DI-water reached almost the same value for the three cycles and demonstrated less variation compared to that of gaseous CO<sub>2</sub> (Fig. 5).

An example of hysteresis in fracture permeability is presented in Figure 6. It depicts the compression and decompression behavior of fracture permeability for gaseous CO<sub>2</sub> and deionized water when pore pressure and pressure gradient across the sample was kept constant at 2 MPa. During unloading (decompression) cycle, permeability values are consistently lower than the loading stage (Fig. 6). A semi-parallel compression curve for fracture permeability is observed for both gaseous CO<sub>2</sub> and DI-water. Throughout the decompression, permeability to the gaseous phase (CO<sub>2</sub>) exhibits a closer trend to loading phase and indicates a lower degree of hysteresis and faster stress release compared to liquid phase (water). When the core plug was unloaded to the initial stress level of about 4.5 MPa, the permeability reached 60% and 72% of its initial value for water and CO<sub>2</sub>, respectively (Fig. 6).

**Time-dependence and fluid effect on fracture permeability**

Figure 7 shows the measured fracture permeability during the test for subsequent injection of water (deionized), CO<sub>2</sub> (gas), and oil (Marcol 52). Fracture permeability to water demonstrates a logarithmic reduction over time, in which 70% of the drop occurs in the first six hours (Fig. 7). Subsequent injection of gaseous CO<sub>2</sub> is accompanied by drying out the liquid phase and a rapid increase of permeability. The flow of oil through the sample indicates a relatively constant value during the experiment. The measured fracture permeability remained approximately constant after forty-eight hours of injection in all three cases.



### Geophysical responses during fracture flow

The results of acoustic velocity and electrical resistivity measurements (both axial and radial directions) are presented in Figures 8. S-wave velocity was only measured in the axial direction. The axial and radial deformations are plotted in Figure 8b. Approximately 0.012 and 0.1 mm (0.031% and 0.13%) changes in diameter and height were recorded respectively during the experiment. Besides the major deformation in phase 1, a reduction in the height and diameter of the sample is observable during the third phase (Fig. 8b). During the initial loading phase, velocity increases almost linearly with the increase of confining pressure and pore pressure (Figs. 8a and 8c). The acoustic velocity remains constant during the second phase until the beginning of phase 3 (Fig. 8c). In the third phase, increasing differential pressure from 3 MPa to 7.5 MPa while pore pressure remained constant resulted in 35-50 m/s (around 1%) increase in radial P-wave velocity ( $V_{pr}$ ), and 80 m/s (1.7%) increase in axial P-wave velocity ( $V_{pa}$ ). Axial S-wave velocity ( $V_{sa}$ ) demonstrates 40 m/s (1.5%) rise throughout the third phase. As a result of increasing differential pressure in the third phase, the  $V_{pa}/V_{sa}$  ratio shows a minute drop from 1.84 to 1.83. During liquid CO<sub>2</sub> injection in the fourth phase,  $V_{pa}$  and  $V_{pr}$  indicate 1.6% (80 m/s) and 0.7% (35 m/s) reduction, while the  $V_{sa}$  decreased around 0.5% (15 m/s). Consequently,  $V_{pa}/V_{sa}$  ratio decreases from 1.83 to 1.80. When looking carefully at the individual radial readings, it appears that  $V_{pr}$  reduces almost simultaneously for the three sensors. Both  $V_{pa}$  and  $V_{pr}$  showed a slight increase when liquid CO<sub>2</sub> injection continued for next twenty-four hours (Fig. 8c).

The electrical resistivity measurements were not performed for phase 1 and a part of phase 2. Figure 8d indicates that electrical resistivity remained almost constant during brine

1  
2  
3  
4  
5  
6  
7  
8  
9  
10  
11  
12  
13  
14  
15  
16  
17  
18  
19  
20  
21  
22  
23  
24  
25  
26  
27  
28  
29  
30  
31  
32  
33  
34  
35  
36  
37  
38  
39  
40  
41  
42  
43  
44  
45  
46  
47  
48  
49  
50  
51  
52  
53  
54  
55  
56  
57  
58  
59  
60

injection of phase 2. After increasing differential pressure in the third phase, both axial and radial resistivity started to increase and leveled off before the end of the phase. The radial measurements follow a similar increasing trend and reflect a higher growth compared to axial one (Fig. 8d). Subsequent injection of liquid CO<sub>2</sub> from the top caused further increase in resistivity. The measurements indicate that the resistivity increased promptly (but with different timings) in three radial levels when CO<sub>2</sub> injection started and remained almost constant during further injection of CO<sub>2</sub>. The increase in electrical resistivity during drainage varies in magnitude for different sensors (about 3-11%).

### DISCUSSION

The performed permeability measurements, small changes in geophysical properties during drainage in addition to the petrographic analysis point out that the fracture is acting as preferential flow pathway in the tested core plug. In particular, measured permeabilities indicate up to two orders of magnitude higher values than the previously reported permeabilities for the matrix (Braathen et al., 2012; Farokhpoor et al., 2014). Therefore, the conducted measurements are reflecting fracture permeability and associated changes in geophysical properties during fracture flow.

#### Fluid flow investigation

Three parameters influence the fracture permeability (Zimmerman and Bodvarsson, 1996; Neuman, 2005; Sahimi, 2011): aperture distribution, roughness and contact area (fraction of fracture surface with zero aperture); changes in stress influence all three. Since the reservoir units in the De Geerdalen Formation are characterized as mechanically competent rocks (Table

2), we expect that the asperities of the fracture surfaces withstand the stress field in our experiments (up to 24 MPa confining pressure). The fracture aperture distribution is heterogeneous (Fig. 4) and the fracture flow is highly stress dependent (Figs. 5 and 6). The increase of confining pressure (burial depth) make the fracture smaller and more heterogeneous by reducing mean aperture, changing surface roughness and broadening variance of aperture distribution (Huo, 2015).

The radial LVDT sensor indicated that an aperture reduction happened during the loading phases (Fig. 8b). Huo and Benson (2015) documented that in addition to aperture size, aperture distribution also changes during loading and unloading cycles. First, the larger apertures get closed at early stress levels, and the contact area continues to increase while confining pressure increases (Huo and Benson, 2015). Hence, the fracture permeability reduction is pronounced at early loading steps as seen in the current study. When the confining pressure is released, aperture size can be restored gradually if the asperities did not experience severe damage during loading. Although permanent damage occurs in rock samples earlier than the maximum compressive strength (Nicksiar and Martin, 2012; Falcon-Suarez et al., 2016b), in this study damage to asperities may not be expected on the tips of asperities because the confining pressure levels are considerably lower than the compressive strength, larger than 135 MPa (Table 2). Because apertures recover slowly and a portion of them remain closed, the fracture permeability values do not reach the preloading values and as a result, show hysteresis (Fig. 6). It is also demonstrated in Figure 6 that the flow of gaseous phase through the fracture causes faster recovery of apertures compared to the liquid phase, which can be associated with higher mobility and compressibility of the gaseous phase. Analysis of x-ray CT scanning revealed that hysteresis is mostly observed in the larger apertures of the fractured samples (Huo, 2015).

The experimental results in Figure 5 suggest that it is necessary to consider stress field, pore pressure inside the fracture, and fluid type when we evaluate the fracture flow properties in a rough-walled fracture. It is shown for a range of confining pressures, which can also be interpreted as different depth levels, that when stress increases fracture permeability decreases as a result of a drop in mechanical and hydraulic aperture and raise in friction factor (from the modified cubic law perspective) (Witherspoon et al., 1980). However, it indicates that different pore pressure levels and fluid types (liquid and gas) can show different flow behaviors. In particular, the distinction is notable at higher stress levels (above 16 MPa) and in early loading stages (below 8 MPa). In addition, Figure 6 demonstrates that in the case of pressure buildup and decompressing a single fracture, the increase in fracture permeability can be a function of stress level and fluid type. While the changes in fracture permeability due to decompression at greater depths are small, the same range of decompression at shallower depth or for more mobile fluid (gas) can bring about higher rates of fracture flow (Fig. 6).

Changes in metastable equilibrium explain the hysteresis phenomenon (Huo and Benson, 2015). The metastability describes a dynamical system that spends an extended time in a state other than the system's least energy configuration. During the metastable configuration with finite lifetime all parameters that characterize the state reach and hold a fixed value. The mechanical strength of the asperities supports the confining stress in a metastable state until the next loading breaks the equilibrium. As the confining pressure increases, the contact area increases that leads to a new metastable equilibrium. The fully elastic recovery of fracture aperture and the extent of hysteresis depend on the mechanical strength of rock and in particular asperities (Table 2). The metastable equilibrium may also explain the time-dependent behavior of fracture flow (Fig. 7). During the oil injection, we expected the least interaction of injectant

1  
2  
3  
4  
5  
6  
7  
8  
9  
10  
11  
12  
13  
14  
15  
16  
17  
18  
19  
20  
21  
22  
23  
24  
25  
26  
27  
28  
29  
30  
31  
32  
33  
34  
35  
36  
37  
38  
39  
40  
41  
42  
43  
44  
45  
46  
47  
48  
49  
50  
51  
52  
53  
54  
55  
56  
57  
58  
59  
60

1  
2  
3  
4  
5  
6  
7  
8  
9  
10  
11  
12  
13  
14  
15  
16  
17  
18  
19  
20  
21  
22  
23  
24  
25  
26  
27  
28  
29  
30  
31  
32  
33  
34  
35  
36  
37  
38  
39  
40  
41  
42  
43  
44  
45  
46  
47  
48  
49  
50  
51  
52  
53  
54  
55  
56  
57  
58  
59  
60

with the core material. As a result, the fracture permeability remains constant throughout oil injection. The significant drop in the fracture permeability during water injection is probably related to the matrix swelling and volumetric strain impact, which caused the relative closure and reduction of fracture aperture. In the more plastic rocks such as coal and organic-rich shale, matrix swelling (volumetric strain) can even result in permanent closure of fracture apertures (Mazumder and Wolf, 2008; Liu and Rutqvist, 2010). Injection of gaseous CO<sub>2</sub> dried the water out of the sample (Fig. 7). While the core plug was drying out during CO<sub>2</sub> injection, the measured fracture permeability increased logarithmically. The value of fracture permeability is almost identical for liquid phases (before swelling) while gaseous CO<sub>2</sub> shows a higher permeability (after drying out). It can be explained by high mobility of gas compared to liquid phases when we consider the flow pathways within the thin and non-uniform fracture aperture along the fractured length (Sahimi, 2011; Kim and Moridis, 2015). Although subsequent injection of fluids could result in two-phase flow for a short period, the measured permeability in 6 hours intervals for two days is considered to be single-phase (or at residual wetting-phase saturation in fracture) because of the limited change in matrix saturation (next section) and the small volume of the fracture saturation. Also, the high rate of injection (1 cm<sup>3</sup>/min) and the elapsed time (48 hours) assured the single-phase flow within the fracture. The investigated sandstone horizon is also prone to long-term geochemical interactions with CO<sub>2</sub>, which can enhance or decimate the porosity-permeability through the dissolution or precipitation of calcite (Ogata et al., 2014).

**Ultrasonic velocity and electrical resistivity observations**

Figure 9 presents the measured and normalized values, as well as the anisotropy in the acoustic velocity and electrical resistivity during the drainage phase. Figures 9a and 9b depict the geophysical measurements during the drainage at phase 4. The acoustic velocity (both  $V_p$  and  $V_s$ ) and electrical resistivity are normalized by the initial brine-saturated condition before injection of  $CO_2$  and are presented in Figures 9c and 9d, respectively. P-wave anisotropy parameter, Thomsen’s epsilon parameter (Thomsen, 1986), is depicted in Figure 9e. Epsilon measures the difference in normal stiffness between vertical and horizontal directions (Sarout and Guéguen, 2008). The electrical resistivity anisotropy is defined as the ratio of radial (horizontal) to axial (vertical) measurements (Wang et al., 2009) and is presented in Figure 9f.

For the vertically fractured De Geerdalen core plug, Figure 9e depicts a close to zero Thomsen’s epsilon parameter. A close to zero epsilon parameter refers to a relatively isotropic medium. During drainage cycle, the P-wave anisotropy parameter decreases at all three levels as  $CO_2$  entered the sample. The magnitude of reduction is almost the same, and a slight buildup is observed towards the end of the cycle. Likewise, Figure 9f illustrates that the anisotropy in electrical resistivity reduces upon introduction of  $CO_2$  into the fractured core. The resistivity anisotropy then stays constant (Fig. 9f). The normalized velocity measurements depict that all three  $V_{pr}$  and  $V_{sa}$  follow a close trend with a minor reduction during  $CO_2$  injection (Fig. 9c). The sensitivity of  $V_{pa}$  to  $CO_2$  fracture flow seems higher compared to other measured velocities (Fig. 9c). On the other hand, the normalized electrical resistivity curves increase abruptly with different values at each radial level (Fig. 9d). Moreover, the axial resistivity measurement shows the highest increase compared to the radial readings towards the end of drainage. The sudden and

1  
2  
3  
4  
5  
6  
7  
8  
9  
10  
11  
12  
13  
14  
15  
16  
17  
18  
19  
20  
21  
22  
23  
24  
25  
26  
27  
28  
29  
30  
31  
32  
33  
34  
35  
36  
37  
38  
39  
40  
41  
42  
43  
44  
45  
46  
47  
48  
49  
50  
51  
52  
53  
54  
55  
56  
57  
58  
59  
60

1  
2  
3  
4  
5  
6  
7  
8  
9  
10  
11  
12  
13  
14  
15  
16  
17  
18  
19  
20  
21  
22  
23  
24  
25  
26  
27  
28  
29  
30  
31  
32  
33  
34  
35  
36  
37  
38  
39  
40  
41  
42  
43  
44  
45  
46  
47  
48  
49  
50  
51  
52  
53  
54  
55  
56  
57  
58  
59  
60

small variation in both acoustic velocity and electrical resistivity supports the dominant fracture flow. Comparison of radial measurements in Figure 9d illustrates that the top radial resistivity sensor detected the CO<sub>2</sub> flow first and the bottom one recorded the variation in resistivity last. Such variation in detecting CO<sub>2</sub> front or similar sensitivity to resistivity cannot be obtained from the acoustic velocity data (Fig. 9c). Furthermore, the modest increase at the end of the drainage phase suggests limited saturation change within the matrix of the rock. The relative position of radial sensors with respect to fracture surface (Fig. 3) could also contribute to different degrees of measured anisotropy. In particular, the bottom sensor had the lowest reading angle with respect to fracture surface while the top one was almost perpendicularly facing the fracture plane.

A cross plot of  $V_p$  versus electrical resistivity is presented in Figure 10. Although it is assumed that the electrical resistivity perpendicular to the bedding (vertical resistivity) is higher than the one parallel to bedding (Wang et al., 2009), it is the radial measurements that span the whole range of the scatter (Fig. 10). However, the highest  $V_p$  is recorded in the axial direction. Injection of CO<sub>2</sub> resulted in the movement of data points toward the bottom right, where electrical resistivity is higher, and acoustic velocity is lower. Since the replaced brine within the De Geerdalen core plug was limited, the recorded geophysical responses show minor variations. Experimental CO<sub>2</sub> flooding of brine-saturated Red Wildmoor, Rothbach and Berea sandstones (Omolo, 2015; Tran, 2015) illustrated that during matrix flow of liquid CO<sub>2</sub> the rate of changes in velocity and resistivity was slower and the magnitude of changes was more substantial compared with the present study. Particularly, it was shown that  $V_p$  decreased 5-15% and electrical resistivity increased 3-5 times (Omolo, 2015; Tran, 2015). Estimation of liquid CO<sub>2</sub> saturation using Archie's equation suggests 65-80% within the matrix of Red Wildmoor,

Rothbach, and Berea clean sandstones (Omolo, 2015; Tran, 2015), while the approximation for overall saturation change within the De Geerdalen sample is about 3-7%.

CONCLUSIONS

To simulate CO<sub>2</sub> flow and sequestration in naturally fractured low-porosity, low-permeability sandstones, we studied a sandstone core plug of the De Geerdalen Formation in the laboratory. Our investigation of stress-dependence and hysteresis of fracture permeability indicated that at higher confining pressures (burial depth) significantly lower permeabilities (even one order of magnitude) is expected for open rough-walled fractures compared to early stress levels. Moreover, pore pressure inside fracture and changes in flow pathway geometry influence the fracture flow both in loading and unloading cycles. It is depicted that gaseous CO<sub>2</sub> may bring about a faster restoration of fracture permeability during decompression compared to the liquid phase. The impact of the fluid type on fracture permeability was found to be notable. Variations in volumetric strain during swelling due to water injection and drying out as a result of CO<sub>2</sub> injection resulted in relative decrease and increase of permeability, respectively. Injection of a non-interacting fluid (Marcol 52 oil) was recorded with steady permeability values.

Geophysical monitoring of brine-CO<sub>2</sub> fracture flow documented the changes in acoustic velocity and electrical resistivity when the contribution of matrix flow is negligible. Axial P-wave velocity and axial resistivity indicated the highest sensitivity to saturation change compared to the axial S-wave velocity, radial V<sub>p</sub>, and radial resistivity when liquid CO<sub>2</sub> displaced brine in the fracture. A minor reduction of P-wave anisotropy (Thomsen's epsilon parameter) is observed during CO<sub>2</sub> injection. Likewise, the anisotropy in electrical resistivity reduced upon introduction of CO<sub>2</sub> into the fractured core. While the front of CO<sub>2</sub> flow through

1  
2  
3  
4  
5  
6  
7  
8  
9  
10  
11  
12  
13  
14  
15  
16  
17  
18  
19  
20  
21  
22  
23  
24  
25  
26  
27  
28  
29  
30  
31  
32  
33  
34  
35  
36  
37  
38  
39  
40  
41  
42  
43  
44  
45  
46  
47  
48  
49  
50  
51  
52  
53  
54  
55  
56  
57  
58  
59  
60



1  
2  
3  
4  
5  
6  
7  
8  
9  
10  
11  
12  
13  
14  
15  
16  
17  
18  
19  
20  
21  
22  
23  
24  
25  
26  
27  
28  
29  
30  
31  
32  
33  
34  
35  
36  
37  
38  
39  
40  
41  
42  
43  
44  
45  
46  
47  
48  
49  
50  
51  
52  
53  
54  
55  
56  
57  
58  
59  
60

the fracture was detected by radial resistivity sensors, the radial  $V_p$  measurements could not record the same observation. An estimated overall 3-7% saturation change within the De Geerdalen sample caused 1.6% and 11% change in axial  $V_p$  and axial electrical resistivity, respectively. The experimental results recorded steeper change and considerably smaller variation of geophysical responses during  $\text{CO}_2$  fracture flow compared to previously published matrix flow measurements. The small changes of acoustic velocity suggest that the use of electrical resistivity methods is crucial for  $\text{CO}_2$  plume monitoring when fracture flow is dominant within the fractured tight reservoirs. It is shown that monitoring using electrical techniques may have the advantage of better detectability and higher sensitivity for geological  $\text{CO}_2$  storage.

#### ACKNOWLEDGMENTS

The authors would like to thank the RCN (Research Council of Norway) funded FME-SUCCESS Centre (subsurface  $\text{CO}_2$  storage - critical elements and superior strategies) and the UNIS (University Centre in Svalbard)  $\text{CO}_2$  Field Laboratory for supporting the research. We appreciate UNIS for providing the core sample. The authors thank Magnus Soldal, Lameck Omondi Omolo and Heidi Debreczeny Wilkinson for their support in performing laboratory experiments. The authors express gratitude to the associate editor and anonymous reviewers for their constructive comments and suggestions that contributed to improving this manuscript.

## REFERENCES

- Alemu, B. L., E. Aker, M. Soldal, Ø. Johnsen, and P. Aagaard. 2013, Effect of sub-core scale heterogeneities on acoustic and electrical properties of a reservoir rock: a CO<sub>2</sub> flooding experiment of brine saturated sandstone in a computed tomography scanner. *Geophysical Prospecting*, **61**, no. 1, 235-250. doi: 10.1111/j.1365-2478.2012.01061.x.
- Arts, R., Winthagen, P., 2005. Monitoring options for CO<sub>2</sub> storage. In: Thomas, D., Benson, S.M. (Eds.), *Carbon Dioxide Capture for Storage in Deep Geologic Formations—Results from the CO<sub>2</sub> Capture Project*, vol. 2. Elsevier, Oxford, pp. 1001–1013.
- Berkowitz, B., 2002, Characterizing flow and transport in fractured geological media: A review. *Advances in Water Resources*, **25**, 861-884.
- Blaisonneau, A., Peter-Borie, M., Gentier, S. 2016, Evolution of fracture permeability with respect to fluid/rock interactions under thermohydraulic conditions: Development of experimental reactive percolation tests. *Geothermal Energy*, **4(1)**, 3. doi:10.1186/s40517-016-0045-9
- Bohloli, B., E. Skurtveit, L. Grande, G. O. Titlestad, M. H. Børresen, Ø. Johnsen, A. Braathen, and A. Braathen. 2014, Evaluation of reservoir and cap-rock integrity for the longyearbyen CO<sub>2</sub> storage pilot based on laboratory experiments and injection tests. *Norsk Geologisk Tidsskrift*, **94**, no. 2-3, 171-187.
- Braathen, A., K. Bælum, H. H. Christiansen, T. Dahl, O. Eiken, H. Elvebakk, F. Hansen, T. H. Hanssen, M. Jochmann, T. A. Johansen, H. Johnsen, L. Larsen, T. Lie, J. Mertes, A. Mørk, M. B. Mørk, W. Nemeč, S. Olaussen, V. Oye, K. Rød, G. O. Titlestad, J. Tveranger, and K. Vagle. 2012, The Longyearbyen CO<sub>2</sub> Lab of Svalbard, Norway—initial assessment of the geological conditions for CO<sub>2</sub> sequestration. *Norwegian Journal of Geology*, **92**, no. 4, 353-376.
- Chen, H., S. Yang, K. Huan, F. Li, W. Huang, A. Zheng, and X. Zhang. 2013, Experimental study on monitoring CO<sub>2</sub> sequestration by conjoint analysis of the P-wave velocity and amplitude. *Environ Sci Technol*, **47**, no. 17, 10071-10077. doi: 10.1021/es4017409.
- Choi, J.C., L. Grande, J. Park, N.H. Mondol. 2017. Anisotropy resistivity measurement using Modified Triaxial Cell: Estimation of geometry factor using numerical simulation. 4th International Workshop on Rock Physics, Trondheim, Norway, 29 May – 2 June 2017.
- Falcon-Suarez, I., L. North, K. Amalokwu, and A. Best. 2016a, Integrated geophysical and hydromechanical assessment for CO<sub>2</sub> storage: shallow low permeable reservoir sandstones. *Geophysical Prospecting*, **64**, no. 4, 828-847. doi: 10.1111/1365-2478.12396.
- Falcon-Suarez, I., Canal-Vila, J., Delgado-Martin, J., North, L., Best, A. 2016b, Characterisation and multifaceted anisotropy assessment of Corvio sandstone for geological CO<sub>2</sub> storage studies. *Geophysical Prospecting*. doi: 10.1111/1365-2478.12469.
- Farokhpour, R., B. J. A. Bjørkvik, E. Lindeberg, and O. Torsæter. 2013, Wettability behaviour of CO<sub>2</sub> at storage conditions. *International Journal of Greenhouse Gas Control*, **12**, 18-25. doi: 10.1016/j.ijggc.2012.11.003.
- Farokhpour, R., E. G. B. Lindeberg, O. Torsæter, M. B. Mørk, and A. Mørk. 2014, Permeability and relative permeability measurements for CO<sub>2</sub>-brine system at reservoir conditions in low permeable sandstones in Svalbard. *Greenhouse Gases: Science and Technology*, **4**, no. 1, 36-52. doi: 10.1002/ghg.1375.

- 1  
2  
3  
4  
5  
6  
7  
8  
9  
10  
11  
12  
13  
14  
15  
16  
17  
18  
19  
20  
21  
22  
23  
24  
25  
26  
27  
28  
29  
30  
31  
32  
33  
34  
35  
36  
37  
38  
39  
40  
41  
42  
43  
44  
45  
46  
47  
48  
49  
50  
51  
52  
53  
54  
55  
56  
57  
58  
59  
60
- Firouzi, M., and J. Wilcox. 2013, Slippage and viscosity predictions in carbon micropores and their influence on CO<sub>2</sub> and CH<sub>4</sub> transport. *J Chem Phys*, **138**, no. 6,064705. doi: 10.1063/1.4790658.
- Huo, D. 2015, Measuring fracture aperture and water saturation distributions using computed tomography and its application to modeling geomechanical impact on fluid flow in fractures, Stanford University.
- Huo, D., and S. M. Benson. 2015, An Experimental Investigation of Stress-Dependent Permeability and Permeability Hysteresis Behavior in Rock Fractures, *Fluid Dynamics in Complex Fractured-Porous Systems*: John Wiley & Sons, Inc. 99-114.
- Kampman, N., Bickle, M., Wigley, M., Dubacq, B. 2014, Fluid flow and CO<sub>2</sub>-fluid-mineral interactions during CO<sub>2</sub>-storage in sedimentary basins. *Chemical Geology*, **369**, 22-50.
- Kim, J., and Moridis, G.J. 2015, Numerical analysis of fracture propagation during hydraulic fracturing operations in shale gas systems, *International Journal of Rock Mechanics and Mining Sciences*, **76**, 127-137.
- Lei, X., and Z. Xue. 2009, Ultrasonic velocity and attenuation during CO<sub>2</sub> injection into water-saturated porous sandstone: Measurements using difference seismic tomography. *Physics of the Earth and Planetary Interiors*, **176**, no. 3-4,224-234. doi: 10.1016/j.pepi.2009.06.001.
- Liu, H. H., and J. Rutqvist. 2010, A new coal-permeability model: Internal swelling stress and fracture-matrix interaction. *Transport in Porous Media*, **82**, no. 1,157-171. doi: 10.1007/s11242-009-9442-x.
- Magnabosco, C., A. Braathen, and K. Ogata. 2014, Permeability model of tight reservoir sandstones combining core-plug and minipermeability analysis of drillcore; longyearbyen co2lab, Svalbard. *Norsk Geologisk Tidsskrift*, **94**, no. 2-3,189-200.
- Mazumder, S., and K. H. Wolf. 2008, Differential swelling and permeability change of coal in response to CO<sub>2</sub> injection for ECBM. *International Journal of Coal Geology*, **74**, no. 2,123-138. doi: 10.1016/j.coal.2007.11.001.
- Moghadam, J. N., N. H. Mondol, P. Aagaard, and H. Hellevang. 2016, Effective stress law for the permeability of clay-bearing sandstones by the Modified Clay Shell model. *Greenhouse Gases: Science and Technology*, **6**, no. 6,752-774. doi: 10.1002/ghg.1612.
- Mørk, M. B. E. 2013, Diagenesis and quartz cement distribution of low-permeability Upper Triassic–Middle Jurassic reservoir sandstones, Longyearbyen CO<sub>2</sub> lab well site in Svalbard, Norway. *AAPG Bulletin*, **97**, no. 4,577-596. doi: 10.1306/10031211193.
- Nakagawa, S., T.J., Kneafsey, T.M. Daley, B.M. Freifeld, and E.V. Rees, 2013, Laboratory seismic monitoring of supercritical CO<sub>2</sub> flooding in sandstone cores using the Split Hopkinson Resonant Bar technique with concurrent x-ray Computed Tomography imaging. *Geophysical Prospecting*, **61(2)**, 254-269.
- Nakatsuka, Y., Z. Xue, H. Garcia, and T. Matsuoka. 2010, Experimental study on CO<sub>2</sub> monitoring and quantification of stored CO<sub>2</sub> in saline formations using resistivity measurements. *International Journal of Greenhouse Gas Control*, **4**, no. 2,209-216. doi: 10.1016/j.ijggc.2010.01.001.
- National Research Council, 1996, *Rock fractures and fluid flow: contemporary understanding and applications*. National Academies Press, Washington, D.C..
- Neuman, S. P. 2005, Trends, prospects and challenges in quantifying flow and transport through fractured rocks. *Hydrogeology Journal*, **13**, no. 1,124-147. doi: 10.1007/s10040-004-0397-2.

- 1  
2  
3  
4  
5  
6  
7  
8  
9  
10  
11  
12  
13  
14  
15  
16  
17  
18  
19  
20  
21  
22  
23  
24  
25  
26  
27  
28  
29  
30  
31  
32  
33  
34  
35  
36  
37  
38  
39  
40  
41  
42  
43  
44  
45  
46  
47  
48  
49  
50  
51  
52  
53  
54  
55  
56  
57  
58  
59  
60
- Nicksiar, M., Martin, C.D. 2012, Evaluation of methods for determining crack initiation in compression tests on low-porosity rocks. *Rock Mechanics and Rock Engineering*, **45(4)**, 607-617.
- Nooraiepour, M., N. H. Mondol, H. Hellevang, and K. Bjørlykke. 2017, Experimental mechanical compaction of reconstituted shale and mudstone aggregates: Investigation of petrophysical and acoustic properties of SW Barents Sea cap rock sequences. *Marine and Petroleum Geology*, **80**,265-292. doi: 10.1016/j.marpetgeo.2016.12.003.
- Ogata, K., K. Senger, A. Braathen, J. Tveranger, and S. Olaussen. 2014, The importance of natural fractures in a tight reservoir for potential CO<sub>2</sub> storage: A case study of the upper Triassic-middle Jurassic Kapp Toscana Group (Spitsbergen, Arctic Norway). In *Geological Society Special Publication*.
- Omolo, L. O. 2015, Experimental study on CO<sub>2</sub> monitoring and saturation with combined acoustic velocity and electrical resistivity in sandstone reservoirs, University of Oslo.
- Pyrak-Nolte, L.J. and J.P. Morris, 2000, Single fractures under normal stress: The relation between fracture specific stiffness and fluid flow. *International Journal of Rock Mechanics and Mining Sciences*, **37(1-2)**, 245-262.
- Pyrak-Nolte, L. J., and D. D.Nolte, 2016, Approaching a universal scaling relationship between fracture stiffness and fluid flow. *Nat. Commun.* 7:10663. doi: 10.1038/ncomms10663
- Rogers, S.F., 2003, Critical stress-related permeability in fractured rocks. *Geological Society Special Publication*, **209**, 7-16.
- Rutqvist, J. 2012, The Geomechanics of CO<sub>2</sub> Storage in Deep Sedimentary Formations. *Geotechnical and Geological Engineering*, 30, no. 3,525-551. doi: 10.1007/s10706-011-9491-0.
- Sahimi, M. 2011, Flow and Transport in Porous Media and Fractured Rock: From Classical Methods to Modern Approaches: Second Edition, Flow and Transport in Porous Media and Fractured Rock: From Classical Methods to Modern Approaches: Second Edition.
- Sarout, J., and Y. Guéguen. 2008, Anisotropy of elastic wave velocities in deformed shales: Part 1 - Experimental results. *Geophysics*, **73**, no. 5,D75-D89. doi: 10.1190/1.2952744.
- Thomsen, L., 1986, Weak elastic anisotropy: *Geophysics*, 51, 1954–1966, doi: 10.1190/1.1442051.
- Tran, T. X. 2015, Monitoring CO<sub>2</sub> behaviour during injection into reservoir sandstone, University of Oslo.
- Wang, Z., L.-J. Gelius, and F.-N. Kong. 2009, Simultaneous core sample measurements of elastic properties and resistivity at reservoir conditions employing a modified triaxial cell - a feasibility study. *Geophysical Prospecting*, **57**, no. 6,1009-1026. doi: 10.1111/j.1365-2478.2009.00792.x.
- Witherspoon, P.A., J.S.Y. Wang, K. Iwai, and J.E. Gale. 1980, Validity of cubic law for fluid-flow in a deformable rock fracture, *Water Resour. Res.*, **16**, 1016-1024.
- Zimmerman, R. W., and G. S. Bodvarsson. 1996, Hydraulic conductivity of rock fractures. *Transport in Porous Media*, **23**, no. 1,1-30.

## CAPTION OF FIGURES

**Figure 1.** Micrographs of the studied De Geerdalen sandstone. (a) optical micrograph of quartz-cemented, low-porosity low-permeability unit, the boxed region expanded in (b) quartz-cement textures such as syntaxial overgrowths on quartz-grains. light= detrital quartz with quartz-cement; darker areas= rock fragments and feldspars; blue= porosity.

**Figure 2.** A schematic representation of the laboratory set-up used in simultaneous fluid flow and geophysical measurements at the Norwegian Geotechnical Institute (NGI).

**Figure 3.** The relative position of three pairs of radial sensors and one radial displacement transducer with respect to the fracture surface; (a) top view; (b) side view.

**Figure 4.** Illustrations of the studied naturally fractured De Geerdalen sandstone core plug. (a) optical image; (b) micro-CT scan; (c) fracture plane extracted from CT scanning. An interpreted fracture aperture plot of the sample before (d) and after (e) the experiment.

**Figure 5.** Stress dependence of fracture permeability. (a) gaseous CO<sub>2</sub>; (b) deionized water.

**Figure 6.** A plot of hysteresis in the fracture permeability for gaseous CO<sub>2</sub> and deionized water.

**Figure 7.** Influence of fluid nature on the fracture permeability observed for gaseous CO<sub>2</sub>, deionized water and oil (Marcol 52).

**Figure 8.** Simultaneous fluid flow and geophysical monitoring. (a) four phases of the experiment, and the corresponding values for confining pressure, pore pressure and differential pressure; (b) changes in height and diameter; (c) acoustic velocity measurements; (d) electrical resistivity measurements.

**Figure 9.** Changes in acoustic velocity and electrical resistivity during drainage of brine by CO<sub>2</sub> in the fracture. (a) acoustic wave velocity measurements; (b) electrical resistivity measurements; (c) normalized acoustic velocity; (d) normalized electrical resistivity; (e) P-wave anisotropy parameter; and (f) electrical resistivity anisotropy.

**Figure 10.** A cross plot of P-wave velocity versus electrical resistivity during the drainage phase.

1  
2  
3  
4  
5  
6  
7  
8  
9  
10  
11  
12  
13  
14  
15  
16  
17  
18  
19  
20  
21  
22  
23  
24  
25  
26  
27  
28  
29  
30  
31  
32  
33  
34  
35  
36  
37  
38  
39  
40  
41  
42  
43  
44  
45  
46  
47  
48  
49  
50  
51  
52  
53  
54  
55  
56  
57  
58  
59  
60

CAPTION OF TABLES

**Table 1** Properties of tested De Geerdalen sandstone core plug

**Table 2** Rock mechanical properties of De Geerdalen Formation (Bohloli et al. 2014). The experimental characterization was performed on the core plugs acquired from Longyearbyen CO<sub>2</sub> storage pilot project, Svalbard, Norway.

1  
2  
3  
4  
5  
6  
7  
8  
9  
10  
11  
12  
13  
14  
15  
16  
17  
18  
19  
20  
21  
22  
23  
24  
25  
26  
27  
28  
29  
30  
31  
32  
33  
34  
35  
36  
37  
38  
39  
40  
41  
42  
43  
44  
45  
46  
47  
48  
49  
50  
51  
52  
53  
54  
55  
56  
57  
58  
59  
60

LIST OF TABLES

Table 1.

Table 1 Properties of tested De Geerdalen sandstone core plug

Well name	Depth (m)	Fracture type	Height (mm)	Diameter (mm)	Porosity (%)	Matrix permeability (mD)
Dh2	772.37	natural, vertical mode I	76.03	38.26	< 2.5	< 0.001

1  
2  
3  
4  
5  
6  
7  
8  
9  
10  
11  
12  
13  
14  
15  
16  
17  
18  
19  
20  
21  
22  
23  
24  
25  
26  
27  
28  
29  
30  
31  
32  
33  
34  
35  
36  
37  
38  
39  
40  
41  
42  
43  
44  
45  
46  
47  
48  
49  
50  
51  
52  
53  
54  
55  
56  
57  
58  
59  
60



**Table 2.**

**Table 2** Rock mechanical properties of De Geerdalen Formation (Bohloli et al. 2014). The experimental characterization was performed on the core plugs acquired from Longyearbyen CO<sub>2</sub> storage pilot project, Svalbard, Norway.

Formation	Vertical stress (MPa)	Fracture pressure (MPa)	Density (g/cm <sup>3</sup> )		Tensile strength, normal to bedding (MPa)		Unconfined compressive strength (MPa)		Young's modulus (E) (MPa)	
			average	range	average	range	average	range	average	range
De Geerdalen	20.7-24.4	13	2.51	2.49-2.52	10.8	9.84-11.63	139.23	135.1-142.6	29.37	23.3-38

1  
2  
3  
4  
5  
6  
7  
8  
9  
10  
11  
12  
13  
14  
15  
16  
17  
18  
19  
20  
21  
22  
23  
24  
25  
26  
27  
28  
29  
30  
31  
32  
33  
34  
35  
36  
37  
38  
39  
40  
41  
42  
43  
44  
45  
46  
47  
48  
49  
50  
51  
52  
53  
54  
55  
56  
57  
58  
59  
60

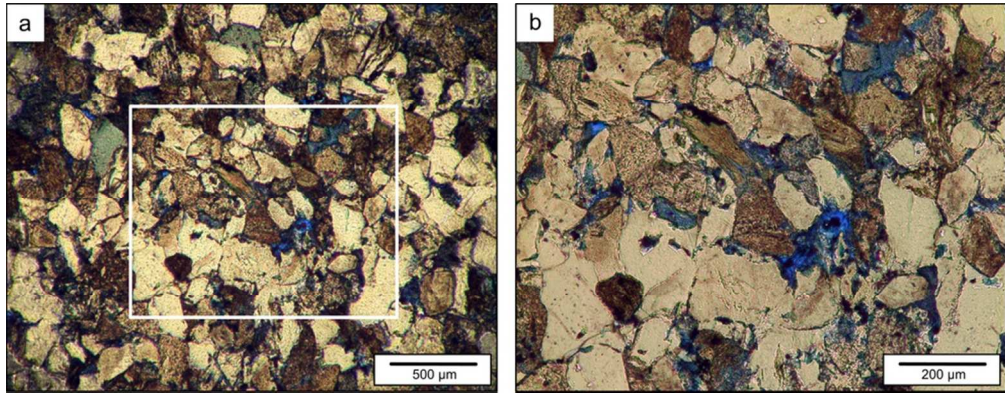


Figure 1. Micrographs of the studied De Geerdalen sandstone. (a) optical micrograph of quartz-cemented, low-porosity low-permeability unit, the boxed region expanded in (b) quartz-cement textures such as syntaxial overgrowths on quartz-grains. light= detrital quartz with quartz-cement; darker areas= rock fragments and feldspars; blue= porosity.

83x32mm (300 x 300 DPI)

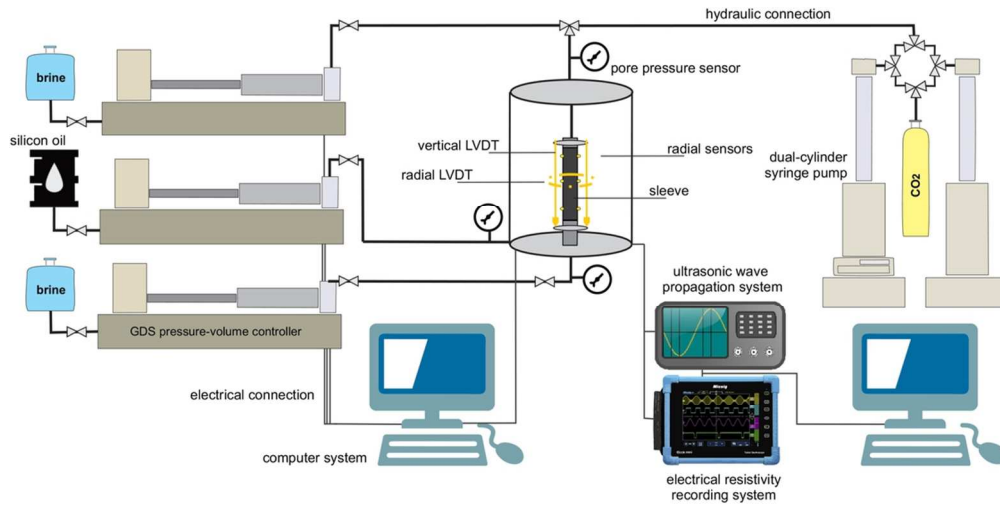


Figure 2. A schematic representation of the laboratory set-up used in simultaneous fluid flow and geophysical measurements at the Norwegian Geotechnical Institute (NGI).

102x50mm (300 x 300 DPI)

1  
2  
3  
4  
5  
6  
7  
8  
9  
10  
11  
12  
13  
14  
15  
16  
17  
18  
19  
20  
21  
22  
23  
24  
25  
26  
27  
28  
29  
30  
31  
32  
33  
34  
35  
36  
37  
38  
39  
40  
41  
42  
43  
44  
45  
46  
47  
48  
49  
50  
51  
52  
53  
54  
55  
56  
57  
58  
59  
60

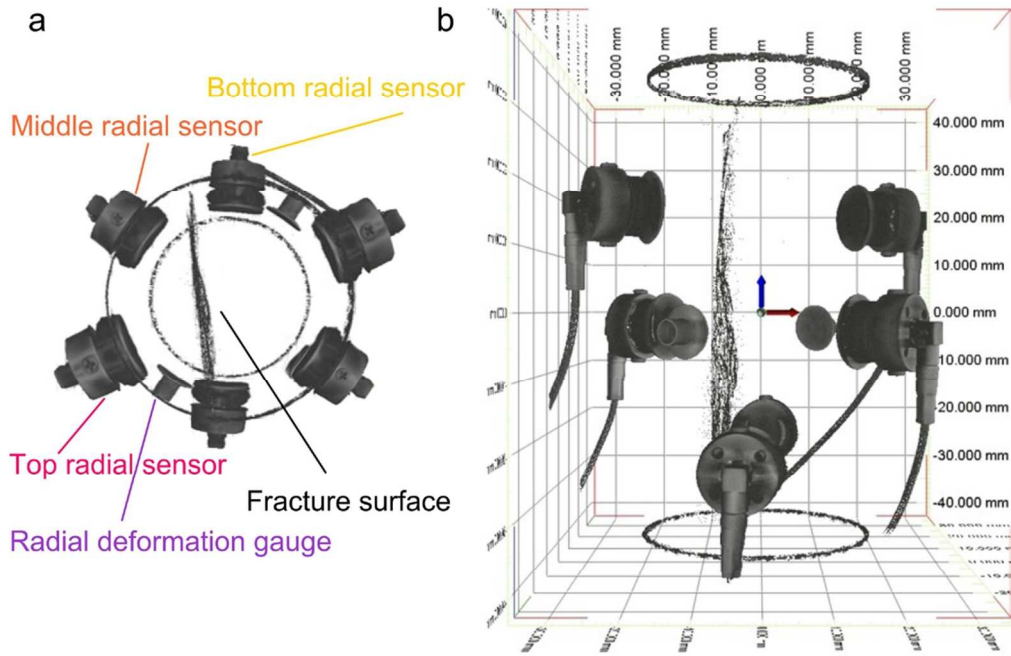


Figure 3. The relative position of three pairs of radial sensors and one radial displacement transducer with respect to the fracture surface; (a) top view; (b) side view.

99x65mm (300 x 300 DPI)

1  
2  
3  
4  
5  
6  
7  
8  
9  
10  
11  
12  
13  
14  
15  
16  
17  
18  
19  
20  
21  
22  
23  
24  
25  
26  
27  
28  
29  
30  
31  
32  
33  
34  
35  
36  
37  
38  
39  
40  
41  
42  
43  
44  
45  
46  
47  
48  
49  
50  
51  
52  
53  
54  
55  
56  
57  
58  
59  
60

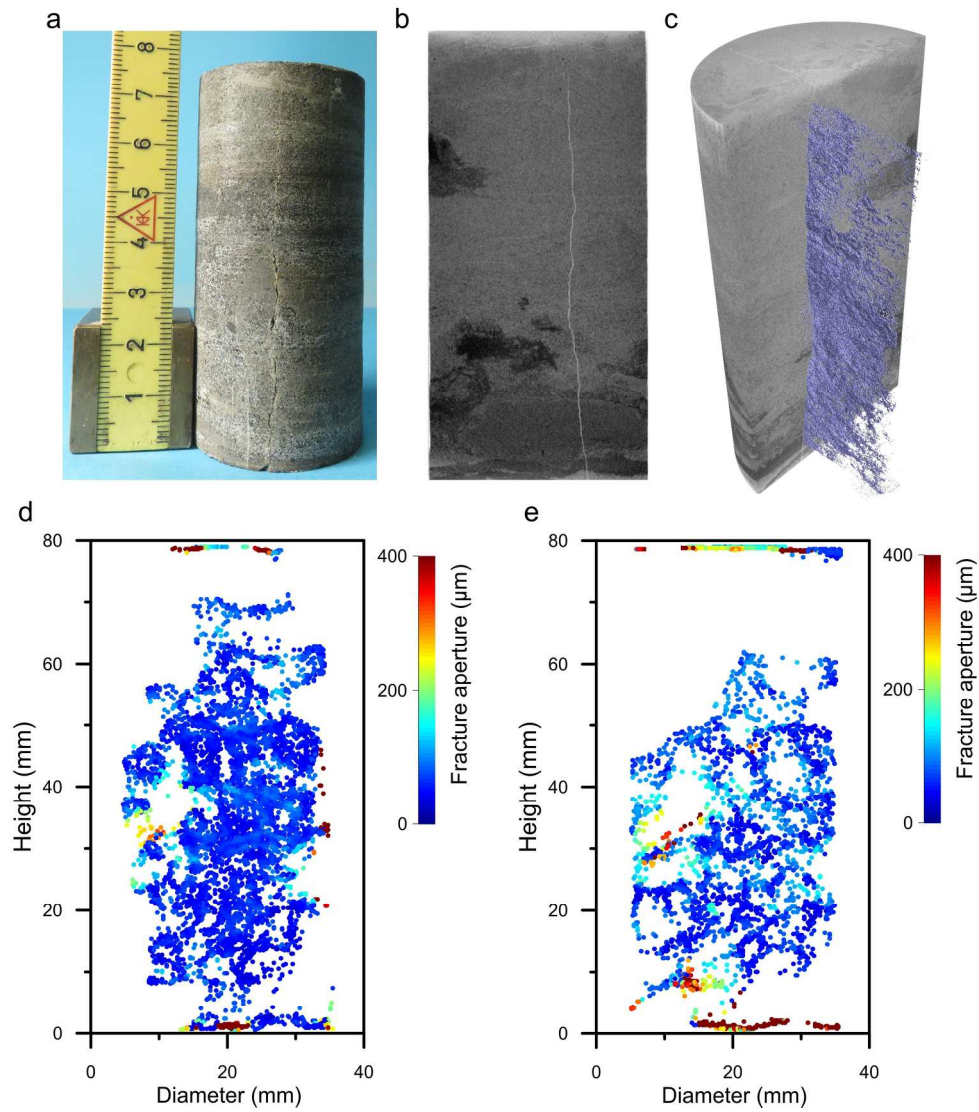


Figure 4. Illustrations of the studied naturally fractured De Geerdalen sandstone core plug. (a) optical image; (b) micro-CT scan; (c) fracture plane extracted from CT scanning. An interpreted fracture aperture plot of the sample before (d) and after (e) the experiment.

200x225mm (300 x 300 DPI)

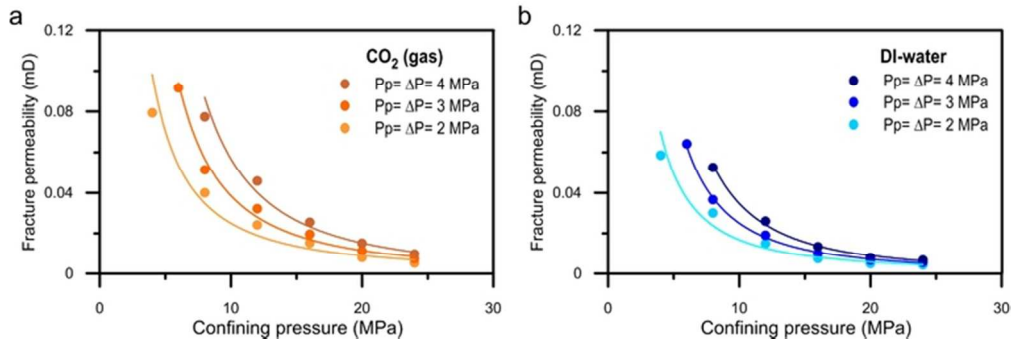


Figure 5. Stress dependence of fracture permeability. (a) gaseous CO2; (b) deionized water.

64x21mm (300 x 300 DPI)

1  
2  
3  
4  
5  
6  
7  
8  
9  
10  
11  
12  
13  
14  
15  
16  
17  
18  
19  
20  
21  
22  
23  
24  
25  
26  
27  
28  
29  
30  
31  
32  
33  
34  
35  
36  
37  
38  
39  
40  
41  
42  
43  
44  
45  
46  
47  
48  
49  
50  
51  
52  
53  
54  
55  
56  
57  
58  
59  
60

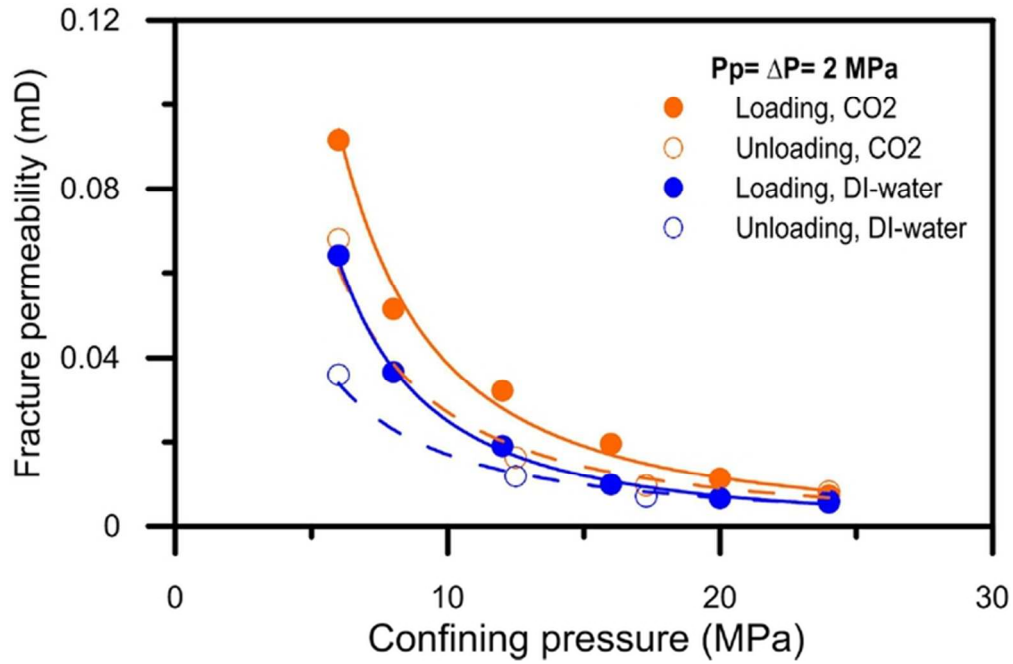


Figure 6. A plot of hysteresis in the fracture permeability for gaseous CO2 and deionized water.

60x39mm (300 x 300 DPI)

1  
2  
3  
4  
5  
6  
7  
8  
9  
10  
11  
12  
13  
14  
15  
16  
17  
18  
19  
20  
21  
22  
23  
24  
25  
26  
27  
28  
29  
30  
31  
32  
33  
34  
35  
36  
37  
38  
39  
40  
41  
42  
43  
44  
45  
46  
47  
48  
49  
50  
51  
52  
53  
54  
55  
56  
57  
58  
59  
60

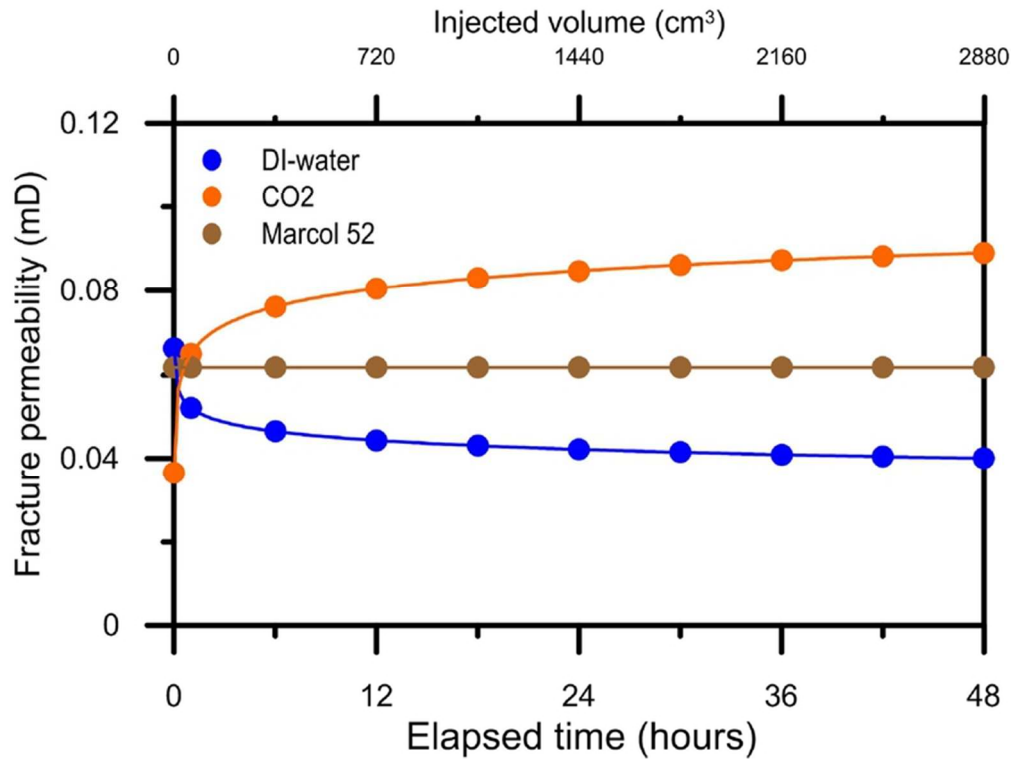


Figure 7. Influence of fluid nature on the fracture permeability observed for gaseous CO2, deionized water and oil (Marcol 52).

69x52mm (300 x 300 DPI)

1  
2  
3  
4  
5  
6  
7  
8  
9  
10  
11  
12  
13  
14  
15  
16  
17  
18  
19  
20  
21  
22  
23  
24  
25  
26  
27  
28  
29  
30  
31  
32  
33  
34  
35  
36  
37  
38  
39  
40  
41  
42  
43  
44  
45  
46  
47  
48  
49  
50  
51  
52  
53  
54  
55  
56  
57  
58  
59  
60



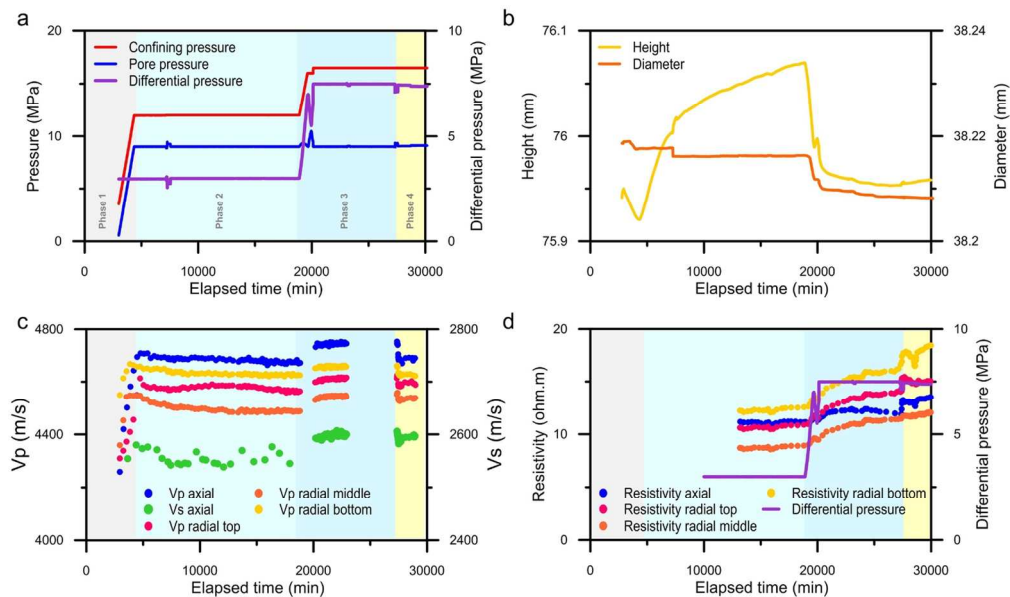


Figure 8. Simultaneous fluid flow and geophysical monitoring. (a) four phases of the experiment, and the corresponding values for confining pressure, pore pressure and differential pressure; (b) changes in height and diameter; (c) acoustic velocity measurements; (d) electrical resistivity measurements.

130x77mm (300 x 300 DPI)

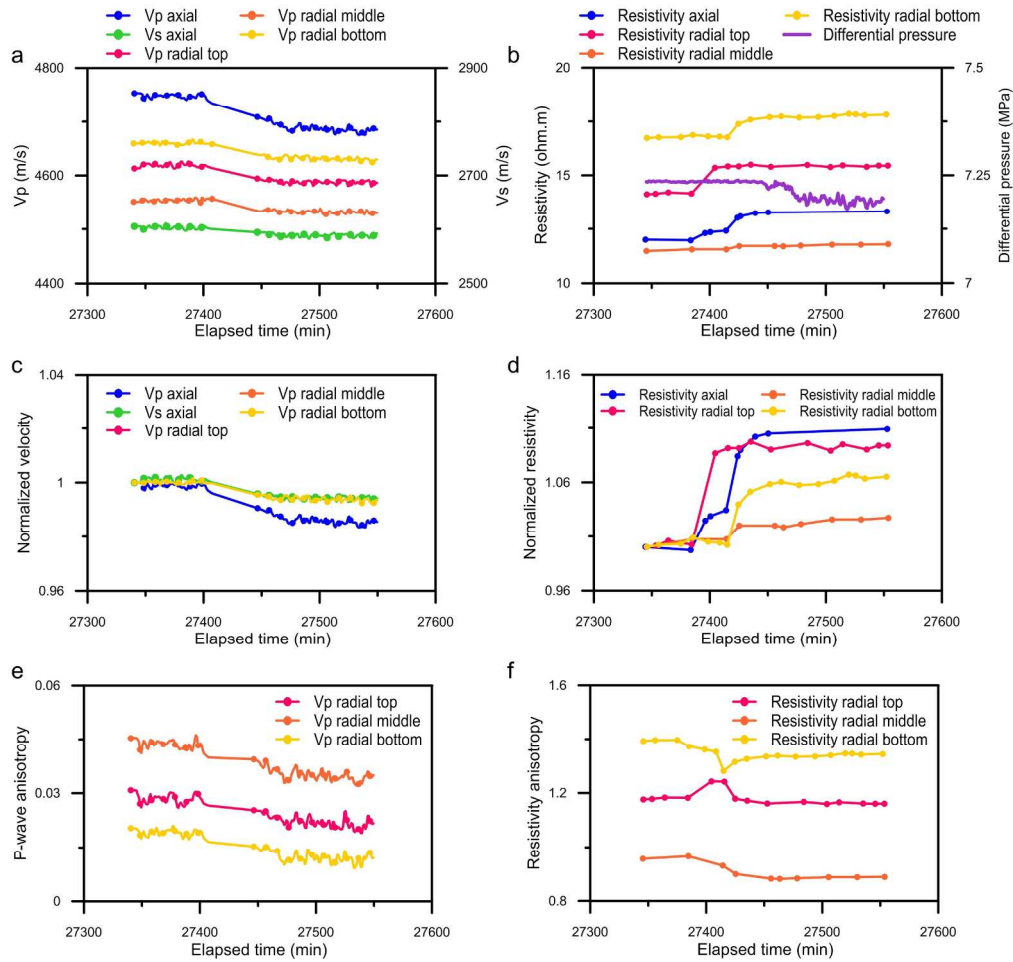


Figure 9. Changes in acoustic velocity and electrical resistivity during drainage of brine by CO<sub>2</sub> in the fracture. (a) acoustic wave velocity measurements; (b) electrical resistivity measurements; (c) normalized acoustic velocity; (d) normalized electrical resistivity; (e) P-wave anisotropy parameter; and (f) electrical resistivity anisotropy.

206x198mm (300 x 300 DPI)

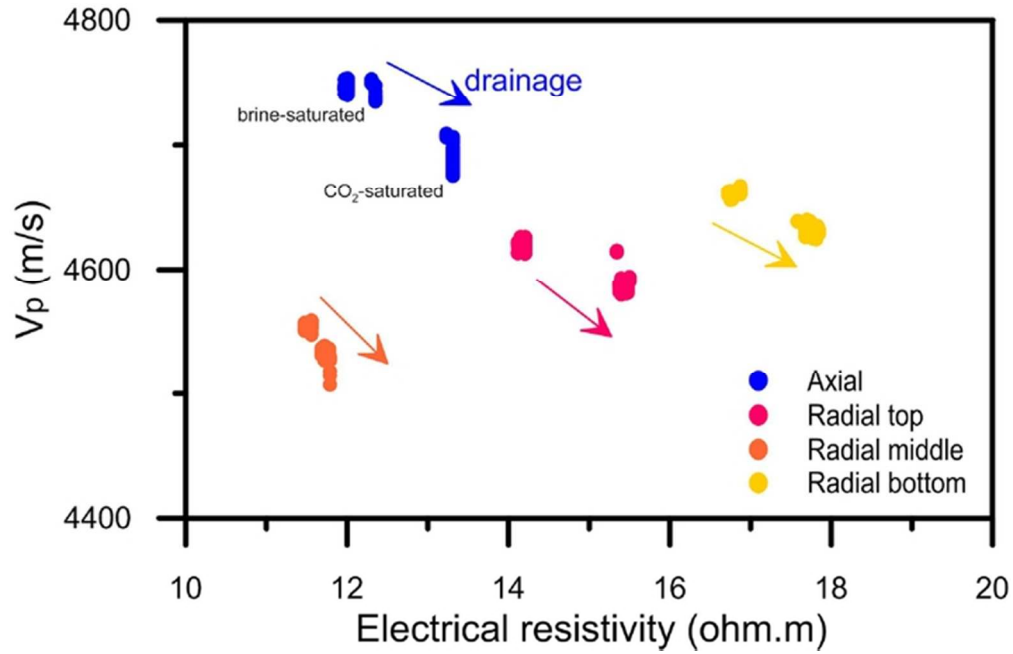


Figure 10. A cross plot of P-wave velocity versus electrical resistivity during the drainage phase.

60x39mm (300 x 300 DPI)

1  
2  
3  
4  
5  
6  
7  
8  
9  
10  
11  
12  
13  
14  
15  
16  
17  
18  
19  
20  
21  
22  
23  
24  
25  
26  
27  
28  
29  
30  
31  
32  
33  
34  
35  
36  
37  
38  
39  
40  
41  
42  
43  
44  
45  
46  
47  
48  
49  
50  
51  
52  
53  
54  
55  
56  
57  
58  
59  
60